3D network single-phase Ni0.9Zn0.1O as anode materials for lithium-ion batteries

Huang, Guoyong; Guo, Xueyi; Cao, Xiao; Tian, Qinghua; Sun, Hongyu

Published in:
Nano Energy

Link to article, DOI:
10.1016/j.nanoen.2016.08.050

Publication date:
2016

Document Version
Peer reviewed version

3D Network Single-phase $Ni_{0.9}Zn_{0.1}O$ as Anode Materials for Lithium-Ion Batteries

Guoyong Huang [a], *Xueyi Guo* [a,*], *Xiao Cao* [a], *Qinghua Tian* [a], *Hongyu Sun* [b]

[a] School of Metallurgy and Environment, Central South University, Changsha 410083, China

[b] Department of Micro- and Nanotechnology, Technical University of Denmark, Kongens Lyngby 2800, Denmark

ABSTRACT: A novel 3D network single-phase $Ni_{0.9}Zn_{0.1}O$ has been designed and synthesized by calcining a special metal-organic precursor (MOP) ($MeO_2C_3H_6$, Me = Ni and Zn, the molar ratio of Ni:Zn = 9:1) as the self-sacrificing template for the first time. Comparing with NiO or the mixture of NiO and ZnO, the new two-step Li-ion storage mechanism in the 3D network single-phase $Ni_{0.9}Zn_{0.1}O$ has been discovered and verified to be: a reversible conversion reaction between $Ni_{0.9}Zn_{0.1}O$ and Ni-Zn alloy ($Ni_{0.9}Zn_{0.1}$), and a reversible Li-alloying reaction between Ni-Zn alloy and $Ni_{0.9}Zn_{0.1}Li$. More remarkably, due to the new mechanism, the anode material shows a low initial discharge platform around ~ 0.5 V (*vs*. Li^+/Li). The first discharge voltage is lower than typical transition-metal oxides, which generally have higher initial discharge plateau around 1.0 V (*vs*. Li^+/Li). It is shown that the novel 3D network single-phase $Ni_{0.9}Zn_{0.1}O$ has outstanding electrochemical performances, demonstrating discharge capacities (*e. g.* 1465.3 $mAhg^{-1}$ at 100 mAg^{-1} and 1055.6 $mAhg^{-1}$ at 800 mAg^{-1}, respectively), excellent capacity

retention and superior rate capability (*e. g.* capacity retention ratio of 92.9% after 150 cycles at 800 mAg^{-1} current density).

KEYWORDS: bi-metal-oxide, metal-organic precursor, 3D network structure, Li-ion storage mechanism, lithium-ion batteries

INTRODUCTION

At present, reducing CO_2 emissions, increasing renewable energy, and improving energy efficiency are the guidelines and requirements of environmental sustainability. Among many of them, there are great demand of hybrid electric vehicles (HEVs), electric vehicles (EVs) and large scale energy storages, specifically. It requires the development of high performance Li-ion batteries (LIBs) in terms of cathode, anode, electrolytes *et al.* [1-3]. Metal oxides [4,5] including Co_3O_4 [6,7], NiO [8-10], Fe_2O_3 [11], CuO [12], *et al.* (conversion reaction mechanism) and ZnO [13], SnO_2 [14,15], *et al.* (alloying-dealloying mechanism) have been intensively studied as promising candidates of LIBs anode materials. The oxide materials have high theoretical capacities exceed the commercial graphite's (372 $mAhg^{-1}$). Recently, bi-metal-oxides, a cobalt-based AB_2O_4 with spinel structure, ($NiCo_2O_4$ [16,17], $MnCo_2O_4$ [18,19], $ZnCo_2O_4$ [20], $CuCo_2O_4$ [21], *et al.*) has received enormous attention by its high electronic conductivity, pronounced cycling stability and superior rate-capability than the single-metal oxide Co_3O_4 [22-26]. Since the cobalt metal is expensive and rare, the nickel metal is considered as an alternative to replace the cobalt in the field of bi-metal-oxides. Ni costs low, and has similar chemical property like Co [27,28]. However, differently from Co of the 3+, the main valence state of Ni is the 2+, which makes it difficult to form single-phase bi-metal-oxides similar to the above spinel structure combining other metal elements. Therefore, most of the relevant researches are focused

on the mixed materials with NiO through the synergetic effect between the two components currently [29-32]. For instance, ZnO-NiO hybrid hollow microspheres with a Ni/Zn molar ratio of 2:1.16 deliver a fairly reversible capacity value (~ 700 $mAhg^{-1}$) after 200 cycles @ 100 mAg^{-1} [29]. Porous ZnO-NiO nanofibers with a Ni/Zn molar ratio of 2:1 present a high discharge capacity value (~ 900 $mAhg^{-1}$) after 120 cycles @ 200 mAg^{-1} [30]. Self-assembly of NiO-coated ZnO Nanorods (32.6 wt.% NiO) show an initial discharge capacity value (~ 1000 $mAhg^{-1}$) @ the high rate of 1 C [31]. More remarkably, the design and synthesis of single-phase nickel-based bi-metal-oxides still remain a significant challenge. On the other hand, metal oxides synthesized with the conversion reaction mechanism, mainly transition-metal oxides (*e. g.* Co_3O_4, $NiCo_2O_4$), commonly show the high discharge voltage platform (~ 1.0 V) (*vs.* Li^+/Li), which inhibits their practical application as anodes in LIBs [Eqs. (1) and (2)] [28,32]. Meanwhile, the other kind of metal oxides with the Li-alloying mechanism (*e. g.* ZnO, SnO_2) possesses a low voltage platform (~ 0.5 V) (*vs.* Li^+/Li) [Eqs. (1) and (3)] [33,34]. However, very few reports have been published on the charge/discharge mechanism of the typical bi-metal-oxides constituted by two types of metals (*e. g.* Ni-Zn-O or Co-Sn-O system).

$$Me_xO_y + 2yLi^+ + 2ye^- \rightarrow xMe + yLi_2O \quad (1)$$

$$Me + Li_2O \leftrightarrow MeO + 2Li^+ + 2e^- \quad (2)$$

$$Me + xLi^+ + xe^- \leftrightarrow Li_xMe \quad (3)$$

Basically, the common synthetic method of metal oxides or bi-metal-oxides is the thermal treatment of inorganic metal precursors including $Me(OH)_2$ [35,36], $MeCO_3$ [7,19], $Me(OH)(CO_3)_{0.5}$ [37] and others [38-40] (Me = Co, Ni, Fe, Zn, *et al.*). Interestingly, metal-organic precursors (MOPs), as effective sacrificial precursors of constructing special micro-

architectures, are receiving increasing attention [41-46]. For example, coated with three-dimensional (3D) graphene and prepared by an iron-based metal organic framework (MOF) MIL-88-Fe, Fe_2O_3 delivers a reversible capacity value (~ 750 $mAhg^{-1}$) after 50 cycles @ 200 mAg^{-1} [43]. Carbon-coated ZnO quantum dots (QDs) (~ 3.5 nm), synthesized through one-step controlled pyrolysis of MOP, show good electrochemical performance (~ 1200 $mAhg^{-1}$ after 50 cycles @ 75 mAg^{-1}) [44]. And porous $ZnO/ZnFe_2O_4$ Octahedra powders, synthesized by using an iron-zinc-based MOF, show good cycling stability (~ 1000 $mAhg^{-1}$ after 100 cycles @ a high current density of 500 mAg^{-1}) [46]. CuO/graphene composite synthesized from a Cu-MOF maintains a stable capacity (~ 600 $mAhg^{-1}$) up to 40 cycles @ 0.6 Ag^{-1} [47]. Hence, in order to go beyond the horizon of conventional preparation techniques, it is very important to innovate and design certain new bi-metal-oxide anodes for LIBs through the MOPs due to the high surface area, tunable pore size and controllable structure [44,46].

Herein, in this paper, a novel 3D network $Ni_{0.9}Zn_{0.1}O$ has been designed and synthesized successfully with a simple and special MOP as the self-sacrificing template. More impressively, this Ni-Zn bi-metal-oxide is not the mixture or composite of NiO and ZnO, but a unique single-phase, which is first reported. By evaluating through a series of electrochemical tests, the results show that the Li storage mechanism is obviously different from NiO or the mixture of NiO and ZnO, especially in initial discharge cycle. Due to the different mechanism, the initial voltage platform is lower (~ 0.5 V) than typical transition-metal oxides (~ 1.0 V) (*vs*. Li^+/Li). And what is more, the outstanding electrochemical performance including excellent capacity retention and superior rate capability is also demonstrated.

EXPERIMENTAL SECTION

Materials. All reagents including $Ni(CH_3COO)_2•4H_2O$ (molecular weight 248.84), $Zn(CH_3COO)_2•2H_2O$ (molecular weight 219.51) and 1,3-propanediol (molecular weight 76.10) are in analytical grade.

Materials Preparation. In a typical synthesis, $Ni(CH_3COO)_2•4H_2O$ (2.24 g) and $Zn(CH_3COO)_2•2H_2O$ (0.22 g) were dissolved in 180 mL 1,3-propanediol to form a homogeneous solution with the ultrasonic wave dissolving technique. The mixed solution was transferred into a Teflon-lined stainless steel autoclave (240 mL) for hydrothermal synthesis at 180 °C in an electric oven for 12 h. Then, after washed for 3 cycles by pure ethanol, the green precipitate as a precursor in the autoclave was dried in a vacuum oven at 40 °C for 24 h. Subsequently, the MOP as precursor was thermally treated at 400 °C in air for 12 h with a heating ramp of 2 $°C·min^{-1}$. Light-green powder was obtained after annealed.

Materials Characterization. The X-ray powder diffraction (XRD) patterns were collected by using multipurpose diffractometer (Rigaku, D/Max-2000) with 2theta ranging of 10°-80° at a scanning rate of $1°·min^{-1}$. The Nitrogen adsorption data were carried out by the specific surface area and porosity analyzer (Quantachrome, NOVA 3200e). The functional groups of MOP were determined by Fourier-translation infrared spectrometer (FT-IR) (Perkinelmer, Lambda 950). The Thermogravimetric Analysis (TGA) of MOP was carried out by the thermal analyzer (Netzsch, 409PC) with a temperature range of 50°-700° at a scanning rate of $5°·min^{-1}$. The micro morphologies were investigated by scanning electron microscope (SEM) (TESCAN, MIRA3 and JEOL); while the micro structures were examined by transmission electron microscope (TEM) (FEI, Tecnai G2 F20). Then, the elemental analysis was characterized both by energy dispersive

X-ray spectrometer (EDX) equipped on the SEM device (TESCAN, MIRA3) and inductively coupled plasma atomic emission spectroscopy (ICP-AES) (Baird, PS-6).

Electrochemical Measurements. The electrochemical performance of as-prepared materials was measured through coin cells at 25 °C. The working electrode was composed of 70 wt% active material, 20 wt% acetylene black (ATB), and 10 wt% polytetrafluoroethylene (PTFE) binder, and the reference/counter electrode was lithium metal. In addition, 1 $mol \cdot L^{-1}$ $LiPF_6$ containing ethylene carbonate (EC), diethyl carbonate (DEC), and propylene carbonate (PC) in the volume ratio of 3:1:1 was used as the electrolyte. In each coin cell, the weight of active material was about 2.00~4.00 mg. The cyclic voltammogram (CV) measurements were carried out ranging from 0.01 to 3.00 V (*vs.* Li^+/Li) at a scan rate of 0.1 $mV \cdot s^{-1}$. The galvanostatic charge-discharge testing was conducted on the battery chargers (Land, CT2001A). And the electrochemical impedance spectroscopy (EIS) measurements were performed at 5 mV AC amplitude over the frequency range of 1 MHz - 0.01 Hz under the open-circuit condition by Electrochemical workstation (Princeton, Parstat 2273).

RESULTS AND DISCUSSION

The possible schematic illustration for the synthesis of MOP is shown in Scheme 1. The metallic centers (Ni^{2+} and Zn^{2+}) firstly react with organic linkers (-OH) of 1,3-propanediol, and form a stable metal-organic complex under the hydrothermal condition at a high reaction temperature [Eq. (4)]. Then, the small metal-organic molecules self-assemble into a layered structure, as a result of the intermolecular forces and coordination bond between the cationic systems acting as electron-withdrawing group and organic ligands acting as electron-donating group [48-50]. Subsequently, in order to reduce the interfacial energy, these layers continue to form secondary self-assembly, constructing the 3D network MOP [41,47] (Figure S1). Upon

pyrolysis, the MOP acts as the self-sacrificing template. On the one hand, the metal components serve as an intrinsic metal source to form the special bi-metal-oxide ($Ni_{0.9}Zn_{0.1}O$) under air atmosphere [Eq. (5)]. On the other hand, the morphology and size of the MOP are inherited by the corresponding product with a slow heating ramp and a low reaction temperature.

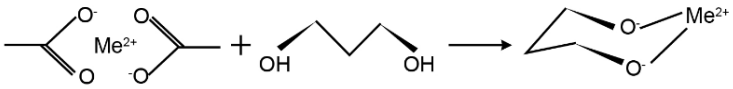

(4)

$$MeO_2C_3H_6 + 4O_2 \rightarrow MeO + 3CO_2 + 3H_2O \quad (5)$$

(Me = Ni and Zn, the molar ratio of Ni:Zn = 9:1)

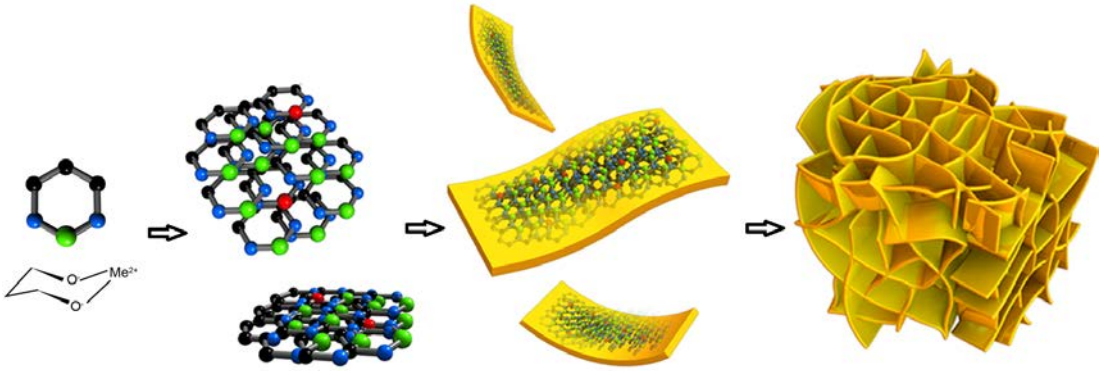

Scheme 1. Possible schematic illustration for the fabrication of MOP.

The main organic functional groups of MOP are analyzed by FT-IR spectrum as shown in Figure 1a. The peaks at ~ 3434 cm^{-1} and ~ 2931 cm^{-1} can be attributed to the stretching vibrations of the Me^{2+}-O^{2-} groups in MOP and the remaining -OH groups in 1,3-propanediol, respectively. And the peak at ~ 1620 cm^{-1} is assigned to the stretching vibration of -CH_2- groups in MOP. Moreover, the peak around 1064 cm^{-1} corresponds to the stretching vibration of the C-O bond in this precursor [51,52]. And the thermal behavior of the MOP is investigated by thermo-gravimetric analysis (TGA) in Figure 1b. The main weight loss of MOP occurs in the temperature ranges of 50-150 °C and 250-350 °C under the air atmosphere, and the total weight

loss of MOP is approximately 39%, which can be ascribed to the transformation of MOP into $Ni_{0.9}Zn_{0.1}O$.

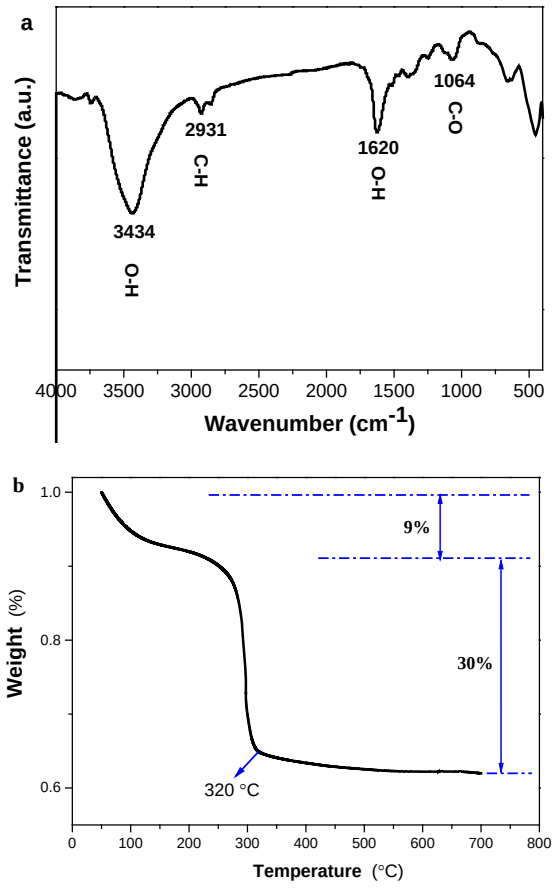

Figure 1. (a) FT-IR spectrum of the as-prepared MOP.Figure and (b) TGA curve of the as-prepared MOP under an air atmosphere (5 °C·min^{-1}).

After calcined, The XRD pattern of the as-prepared sample presents in Figure 2a. The diffraction peaks correspond to the cubic phase $Ni_{0.9}Zn_{0.1}O$ (JCPDS no.75-0270, space group Fm-*3m*, $a = b = c = 4.188$ Å), which is similar to the standard pattern of cubic phase NiO (JCPDS no.71-1179, space group Fm-*3m*, $a = b = c = 4.178$ Å). Nonetheless, it is obviously different from that of the mixture of commercial NiO and ZnO (the molar ratio of Ni:Zn = 9:1) (Figure S2). In addition, a unit cell structure of the $Ni_{0.9}Zn_{0.1}O$ crystal as shown in Figure 2b, the basic tectonic unit is a cube with the oxygen and metal atoms (Ni and Zn) alternately arranging,

while Ni and Zn atoms can randomly substitute each other. Meanwhile, the BET specific surface area is about 270.5 $m^2 \cdot g^{-1}$ calculated by the N_2 adsorption data in Figure S3.

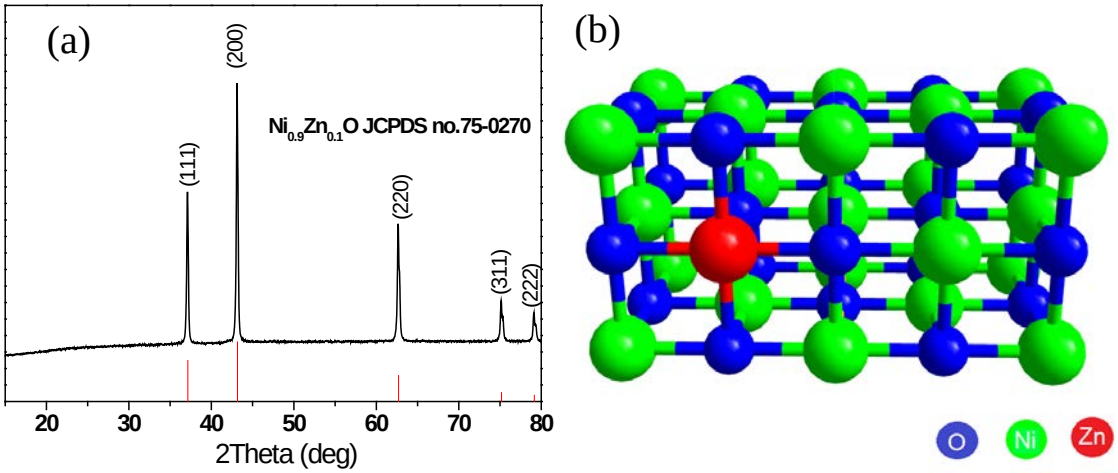

Figure 2. (a) XRD pattern and (b) unit cell of $Ni_{0.9}Zn_{0.1}O$ powders.

The SEM and TEM images are shown in Figure 3. The typical sample shows an interconnected porous 3D network morphology (Figure 3a) self-assembled by many thin layers (10-20 nm) (Figure S4). In addition, the SEM micrograph of the as-prepared sample and the corresponding EDX mapping images of Ni, Zn and O elements are shown in Figure S5. The edges and morphologies of Ni, Zn and O in Figure S5b-S5d are indexed as the morphology shown in Figure S5a. And the concentration distributions of Ni and Zn are ultra uniform. Then, the representative EDX spectrum (Figure S5e) indicates that the Ni:Zn atomic ratio is about 0.902:0.098, which matches well with the theoretical value of $Ni_{0.9}Zn_{0.1}O$. Interestingly, the Ni and Zn quality fractions of the Ni_xZn_yO sample, measured by ICP-AES, are 70.10% and 8.66%, respectively; which agrees well with the EDX result. The 3D $Ni_{0.9}Zn_{0.1}O$ consists of irregular nanosheets is further elucidated by TEM (Figure 3b) as seen from SEM images. Shown in the high-resolution TEM (HRTEM) images (Figures 3c and 3d), the *d*-spacings are measured to be 0.24 nm and 0.15 nm, which are indexed to the (111) and (220) planes of cubic $MnCo_2O_4$, respectively [20,41,53].

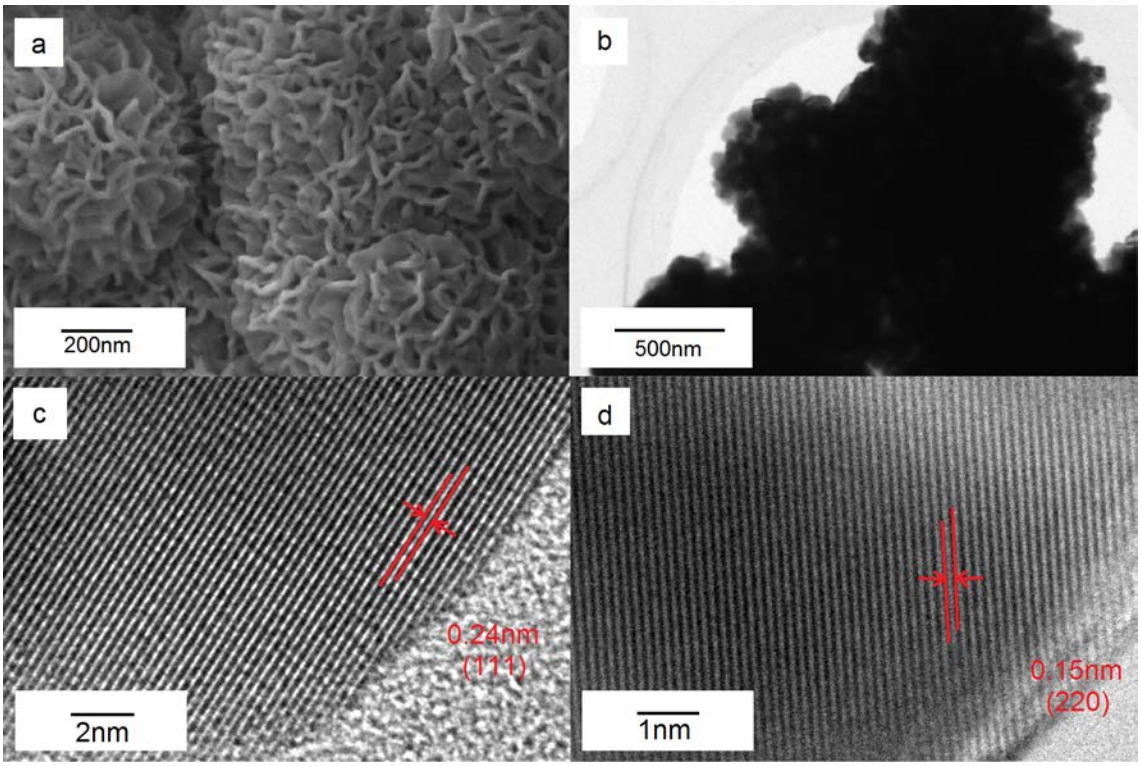

Figure 3. (a) SEM, (b) TEM, (c) and (d) HRTEM images of $Ni_{0.9}Zn_{0.1}O$ powders.

Prompted by the unique single-phase $Ni_{0.9}Zn_{0.1}O$ as anode materials for LIBs firstly, the Li-ion storage mechanism is researched systematically. The initial discharge and charge profiles of the 3D network single-phase $Ni_{0.9}Zn_{0.1}O$ electrodes in the voltage range of 0.01-3.00 V (*vs.* Li^+/Li) at various rates (100, 400 and 800 mAg^{-1}) are shown in Figure 4. Distinctively, in all of the first discharge curves, long plateaus (~ 0.50 V) are clearly observed, which is obviously lower than the typical voltage platform (~ 1.00 V) of pure transition-metal oxides (NiO, CoO, *et al.*) [4,22,28]. Considering the Zn element, its oxide presents a different mechanism of lithium insertion/deinsertion with a low voltage plateau (~ 0.5 V) [51,53,54]. Therefore, a new possible Li-ion storage mechanism of $Ni_{0.9}Zn_{0.1}O$, which is different from either the pure NiO or the mixture of NiO and ZnO [8,29,30], is expressed as follows [Eqs. (6)-(9)]. During the typical initial discharge curve, the reduction process may involve the reduction of $Ni_{0.9}Zn_{0.1}O$ to Ni-Zn alloy ($Ni_{0.9}Zn_{0.1}$) in the first step [Eq. (6)], and then the reaction to form Li-Zn-Ni alloy

($Ni_{0.9}Zn_{0.1}Li$) in the second step [Eq. (7)]. In the subsequent charge curve, the oxidation reaction occurs between $Ni_{0.9}Zn_{0.1}Li$ and $Ni_{0.9}Zn_{0.1}$ in the first step [Eq. (8)], and then the further oxidation forms $Ni_{0.9}Zn_{0.1}O$ in the second step [Eq. (9)]. In addition, the initial discharge capacities at above rates are 1465.3, 1167.9 and 1055.6 $mAhg^{-1}$, respectively; while the corresponding charge capacities are 942.5, 833.9 and 700.7 $mAhg^{-1}$, respectively. The irreversible capacity loss values are between 30% and 35%, which may arise with the formation of SEI layer during the initial discharge [5,42,55]. Because an additional reversible capacity may be contributed by the SEI film formation and the electrolyte decomposition, some of the specific capacities as above are higher than the theoretical capacities of both NiO (718 $mAhg^{-1}$) and ZnO (978 $mAhg^{-1}$) [34,54,56].

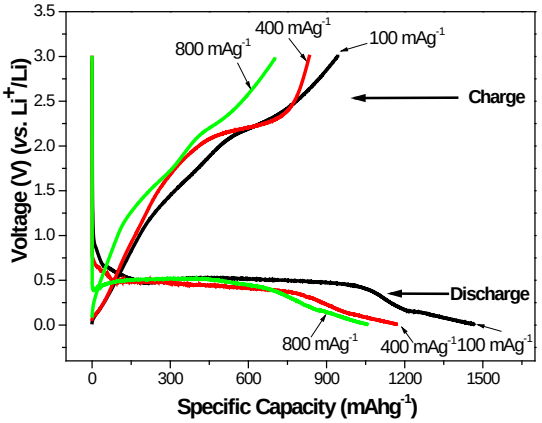

Figure 4. Initial discharge and charge profiles of $Ni_{0.9}Zn_{0.1}O$ electrode in the range of 0.01-3.00 V (*vs.* Li^+/Li) at different rates of 100, 400 and 800 mAg^{-1}.

$$Ni_{0.9}Zn_{0.1}O + 2Li^+ + 2e^- \rightarrow Ni_{0.9}Zn_{0.1} + Li_2O \quad (6)$$

$$Ni_{0.9}Zn_{0.1} + Li^+ + e^- \rightarrow Ni_{0.9}Zn_{0.1}Li \quad (7)$$

$$Ni_{0.9}Zn_{0.1}Li \rightarrow Ni_{0.9}Zn_{0.1} + Li^+ + e^- \quad (8)$$

$$Ni_{0.9}Zn_{0.1} + Li_2O \rightarrow Ni_{0.9}Zn_{0.1}O + 2Li^+ + 2e^- \quad (9)$$

In order to verify this conjecture, the TEM and HRTEM images of $Ni_{0.9}Zn_{0.1}O$ electrode after the initial discharge ranging from 0.01 V to 3.00 V at 100 mAg^{-1} are shown in Figure 5. It can be observed that the 3D network morphology of the active material remains intact in (Figure 5a) and the formation of Zn nanoparticles with diameter in the range of 3-10 nm can be found in Figure 5b. The lattice fringes can be clearly seen from the magnified inset in Figure 5b with the interplane spacing of ~ 0.25nm, which is attributed to the (002) crystalline plane of the Zn metal, corresponding to the above discharge mechanism. To further evaluate the electrochemical mechanism, the first three cyclic voltammogram curves of $Ni_{0.9}Zn_{0.1}O$ electrode were recorded at the scan rate of 0.1 $mV \cdot s^{-1}$ in the range of 0.01-3.00 V in Figure 6. Two pronounced cathodic peaks can be observed at 1.20 V and 0.28 V during the first discharge scan, which may belong to the reduction of $Ni_{0.9}Zn_{0.1}O$ to Ni-Zn alloy [Eq. (6)], and the alloying reaction between Li and Ni-Zn alloy [Eq. (7)], respectively [39,52,57]. And two well-defined anodic peaks are recorded at 0.20 V and 2.24 V during the first charge scan, which may be attributed to the de-alloying of $Ni_{0.9}Zn_{0.1}Li$ to Ni-Zn alloy [Eq. (8)], and the oxidation reaction of Ni-Zn to $Ni_{0.9}Zn_{0.1}O$ [Eq. (9)], respectively [11,26,58]. From the second cycle onwards, the CV profiles remain steady as they do not change significantly upon further sweeps, suggesting highly reversible electrochemical reactions of this material.

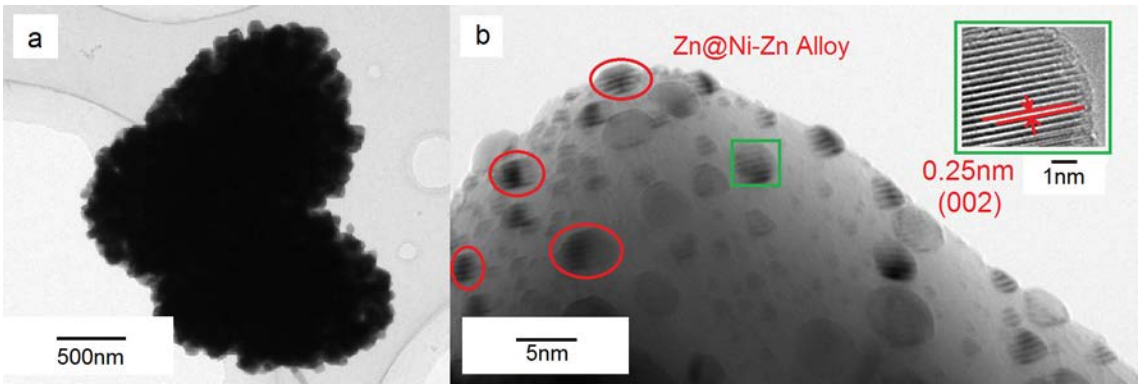

Figure 5. (a) TEM and (b) HRTEM images of $Ni_{0.9}Zn_{0.1}O$ powders after the initial discharge ranging from 0.01 V to 3.00 V (*vs*. Li^+/Li) at 100 mAg^{-1}, and the green rectangle region in panel (b) magnified as an inset.

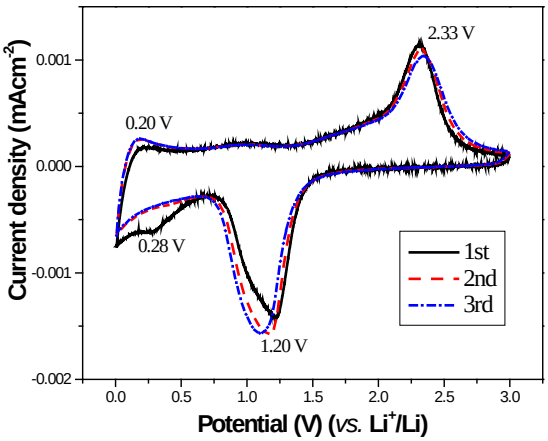

Figure 6. First three cyclic voltammogram curves of $Ni_{0.9}Zn_{0.1}O$ electrode at the scan rate of 0.1 $mV \cdot s^{-1}$ in the range of 0.01-3.00 V (*vs*. Li^+/Li).

Figure 7a represents the systematic cycling performance of 3D network single-phase $Ni_{0.9}Zn_{0.1}O$ electrodes at 400 and 800 mAg^{-1}. Under the low rate (400 mAg^{-1}), the reversible capacity of the initial 10 cycles (except the 1st cycle) decreases slowly and gradually from ~ 830 $mAhg^{-1}$ to ~ 760 $mAhg^{-1}$, which may be ascribed to the formation of the SEI film by consuming a certain amount of active materials [28,59,60]. Then, the reversible capacity keeps constant (750-760 $mAhg^{-1}$) until approximately the 160th cycle, and the charge capacity retention ratio (*vs. the initial charge capacity*) is maintained as 91.6%. During the last 40 cycles, the reversible capacity begins to fall slowly to 610 $mAhg^{-1}$, and the corresponding capacity retention ratio is still about 73.5%. As a contrast, under the high rate (800 mAg^{-1}), the trend of discharge/charge

capacity *vs.* cycle number is very similar to the case of the low rate. For the initial 20 cycles, the reversible capacity declines from ~ 700 $mAhg^{-1}$ to ~ 630 $mAhg^{-1}$; then, the reversible capacity keeps stable (630-660 $mAhg^{-1}$) up to the 150th cycle, and the corresponding capacity retention ratio is up to ~ 92.9%; during the last 50 cycles, the reversible capacity goes down to ~ 450 $mAhg^{-1}$. Except the initial cycles, the stable and good reversibility of the electrochemical processes is also confirmed by the high Coulombic efficiencies, which can be stabilized to ~ 98.5% at 400 mAg^{-1} and ~ 97.3% at 800 mAg^{-1}, respectively. For further investigation of the rate capability, the $Ni_{0.9}Zn_{0.1}O$ electrode was measured at various rates between 400 and 6400 mAg^{-1}. As shown in Figure 7b, the specific capacity fades with the increasing current density, and the ranges of corresponding charge capacity are 771.7-811.7, 643.2-661.8, 491.1-513.7, 263.5-317.6 and 125.9-144.7 $mAhg^{-1}$ at 400, 800, 1600, 3200 and 6400 mAg^{-1}, respectively. However, the reversible capacity goes up from 520.1 $mAhg^{-1}$ to 588.5 $mAhg^{-1}$ when the rate recovers to 800 mAg^{-1}; while it retains to a high specific capacity (~ 680.0 $mAhg^{-1}$) after 120 cycles when the rate goes back to the low current density (400 mAg^{-1}), dramatically. The work's electrochemical performances and other previously reported results are summarized in Table 1. To our knowledge, the 3D network single-phase $Ni_{0.9}Zn_{0.1}O$ material is one of the best with long-term cycling stability and rate capability among various NiO, ZnO, mixtures of NiO/ZnO and ZnO-based electrode materials. Hence, the novel $Ni_{0.9}Zn_{0.1}O$ anode illustrates high reversible capacities, excellent capacity retention and superior rate capability due to: 1) the special Li-ion storage mechanism, 2) the highly acceptable volume expansion accommodated by the large interior space among the network accommodating the volume expansion greatly, and 3) the short diffusion lengths of Li-ions [42,50,61].

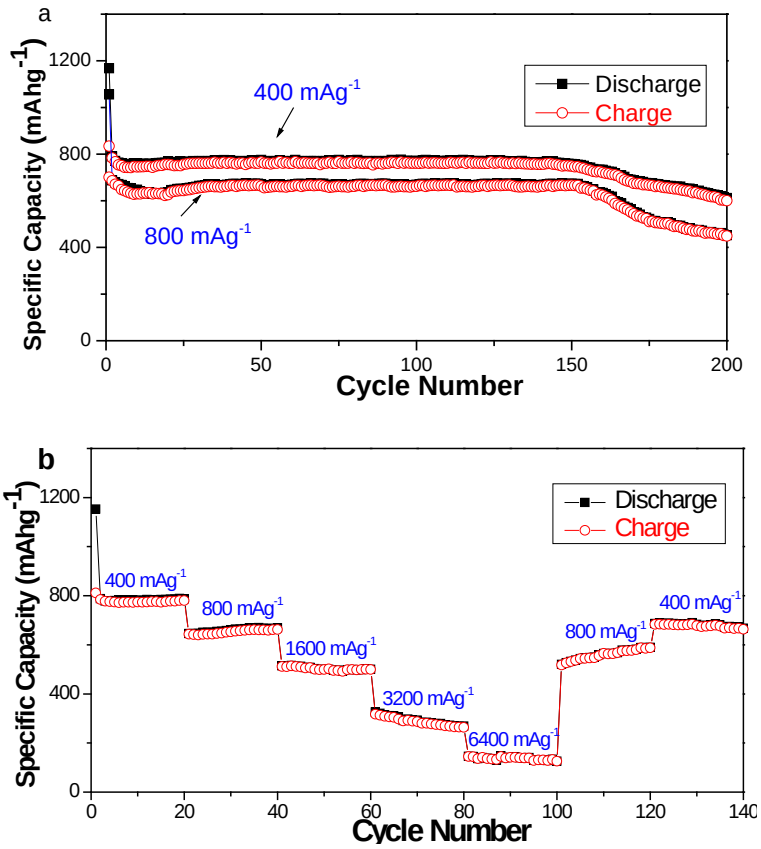

Figure 7. (a) Cycling performance of $Ni_{0.9}Zn_{0.1}O$ electrodes at 400 and 800 mAg^{-1}; (b) Rate capability of $Ni_{0.9}Zn_{0.1}O$ electrode at various rates.

Table 1. Comparison of this work's electrochemical performances and other previously reported results

Electrode material	Morphology	Specific Capacity ($mAhg^{-1}$)	Current density	Cycles	Ref.
$Ni_{0.9}Zn_{0.1}O$	3D network	610.0	400 mAg^{-1}	200	This work
NiO	Nanosheets	800.0	400 mAg^{-1}	150	9
NiO/Carbon	Nanosheets	848.0	400 mAg^{-1}	50	10
NiO/ZnO	Microspheres	1176.0	100 mAg^{-1}	200	29
NiO/ZnO	Nonofibers	949.0	200 mAg^{-1}	120	30
NiO/ZnO	Nanorods	960.0	1 C	15	31
$ZnO/ZnFe_2O_4$	Microcubes	800.0	1000 mAg^{-1}	200	39
ZnO	Quantum dots	~1200.0	75 mAg^{-1}	50	44
ZnO@Si	Nanoparticles	~1500.0	0.05 C	260	57

To gain additional insight into the charge-transfer procedure, the EIS measurements were tested in a frequency range of 1 MHz - 0.01 Hz with the 5 mV AC amplitude after the 1st, 100th and 200th cycle at 800 mAg^{-1} under the open-circuit condition (Figure 8). These Nyquist plots are all composed of a high-frequency semicircle and a low-frequency approximate sloping straight line. The former may be explained as the charge transfer resistance and the SEI resistance; while the latter corresponds to the Warburg impedance relating to the diffusion of lithium-ions [7,35,62]. And the equivalent circuit used to fit the spectra is presented in the inset. In this work, R_s represents the intrinsic resistance of active materials and ionic resistance in electrolyte. R_{sf} and C_{sf} denote the SEI film resistance and the corresponding capacitance, respectively; while R_{ct} and C_{dl} are the charge-transfer resistance and the double-layer capacitance, respectively. In addition, Q represents the constant phase element [31,52]. When the cycling number increases from 1 to 100, the corresponding R_{ct} value is experiencing merely no change in the range of 210.4-240.2 Ω, which shows that the charge transfer resistance value grows up slowly. Until the 200th cycle, the corresponding R_{ct} value increases to 474.8 Ω. To sum up, the $Ni_{0.9}Zn_{0.1}O$ electrode displays a good electrode conductivity, which indicates that doping Zn element may greatly enhance the electronic conductivity of the special bi-metal-oxide [34,63-66]. Remarkably, in Figure 9, the $Ni_{0.9}Zn_{0.1}O$ shows negligible change in morphology after 200 cycles at 800 mAg^{-1}, which displays an attractive stability in micro-structure. So this unique 3D network structure may prevent the particles from fragmentation and agglomeration [42,67-70].

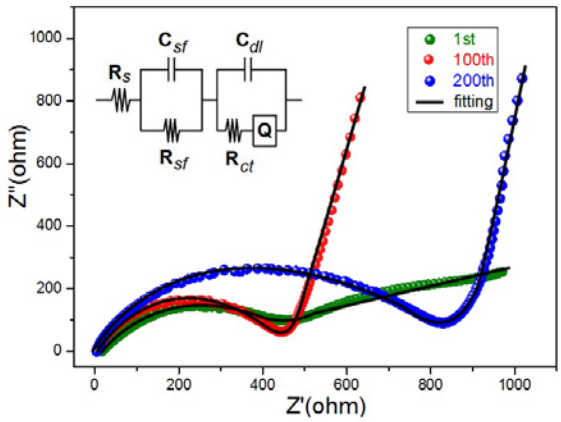

Figure 8. Nyquist plots of the $Ni_{0.9}Zn_{0.1}O$ electrode after different cycles at 800 mAg^{-1} measured with the 5 mV amplitude over the frequency range from 1 MHz to 0.01 Hz under the open-circuit condition. The fitting lines were obtained using the equivalent circuit in the inset.

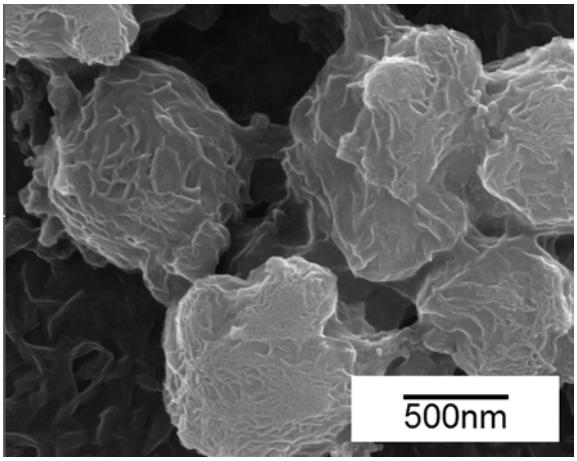

Figure 9. SEM images of the $Ni_{0.9}Zn_{0.1}O$ electrode (the mixture of $Ni_{0.9}Zn_{0.1}O$/ATB/PVDF) after 200 cycles at 800 mAg^{-1}.

CONCLUSIONS

In summary, the novel single-phase $Ni_{0.9}Zn_{0.1}O$ has been designed and synthesized through a special MOP ($MeO_2C_3H_6$, Me = Ni and Zn, the molar ratio of Ni : Zn =9 :1) as the self-sacrificing template. Its unique porous 3D network morphology is self-assembled by many thin layers (10-20 nm), and the specific surface area is about 270.5 $m^2 \cdot g^{-1}$. Comparing with NiO or the mixture of NiO and ZnO, the new two-step Li-ion storage mechanism in the 3D network

single-phase $Ni_{0.9}Zn_{0.1}O$ has been discovered and verified to be: a reversible conversion reaction between $Ni_{0.9}Zn_{0.1}O$ and Ni-Zn alloy ($Ni_{0.9}Zn_{0.1}$), and a reversible Li-alloying reaction between Ni-Zn alloy and $Ni_{0.9}Zn_{0.1}Li$. More remarkably, due to the new mechanism, the anode material shows a low initial discharge platform around ~ 0.5 V (*vs.* Li^+/Li). The first discharge voltage is lower than typical transition-metal oxides, which generally have higher initial discharge plateau around 1.0 V (*vs.* Li^+/Li). In addition, due to the large interior space among the network, the short diffusion lengths of Li-ions, and the doping of active Zn element, it is shown that the novel 3D network single-phase $Ni_{0.9}Zn_{0.1}O$ has outstanding electrochemical performances, demonstrating high discharge capacities (*e. g.* 1465.3 $mAhg^{-1}$ at 100 mAg^{-1} and 1055.6 $mAhg^{-1}$ at 800 mAg^{-1}, respectively), excellent capacity retention and superior rate capability (capacity retention ratio of 91.6% after 160 cycles at low 400 mAg^{-1} current density and 92.9% after 150 cycles at high 800 mAg^{-1}, respectively)

ASSOCIATED CONTENT

Supporting Information

Supplementary data associated with this article can be found in the online version at DOI:XXXX. SEM images of the MOP with different reaction times; XRD pattern of commercial NiO and ZnO powders; N_2 adsorption isotherm of $Ni_{0.9}Zn_{0.1}O$ powders; SEM image of $Ni_{0.9}Zn_{0.1}O$ powders with high magnification; SEM image, corresponding EDX mapping images and representative EDX spectrum of $Ni_{0.9}Zn_{0.1}O$ powders.

ACKNOWLEDGMENT

This work was supported by the National Natural Science Foundation of China (Grant No. 51234009) and the Production, Teaching and Research program of Guangdong province (No. 2013A090100003).

AUTHOR INFORMATION

Corresponding Author

*E-mail: xyguo@csu.edu.cn. Tel.:+86 731 88876255.

Author Photo and Resume

Guoyong Huang received his B.S. (2005) in polymer science and engineering, M.S. (2007) and Ph.D. (2015) in chemical engineering and technology from Tsinghua University in China. He also worked as a researcher at Brunp recycling technology Co., Ltd. (2007-2011). In 2015, he became an assistant professor in the School of Metallurgy and Environment at Central South University. His research interests are focused on synthesis of nanomaterials for energy storage and conversion and recycling waste secondary batteries.

Xueyi Guo received his Ph.D. degree in nonferrous metals from Central South University in 1995. He was a visiting research scholar in the University of Tokyo, Japan, from 2000-2003. Now he is a Full Professor in the School of Metallurgy and Environment at Central South University. His research interests are focused on advanced technology of resources recycling and advanced materials.

Xiao Cao received his B.S. degree in metallurgical engineering from Central South University. Currently, he is a master candidate in the School of Metallurgy and Environment at Central South University. He is interested in synthesis of nanomaterials for energy storage and conversion.

Qinghua Tian received his Ph.D. degree in nonferrous metallurgy from Central South University in 2009. Now he serves as an associate professor in the Scholl of Metallurgy and Environment at Central South University. He has been engaged in the research of hydrometallurgy, nonferrous metal resources recycling and advanced materials.

Hongyu Sun received his Ph.D. degree from State Key Laboratory of Metastable Materials Science and Technology in Yanshan University in 2010. After that, he spent 2 years as a postdoctoral researcher in the Department of Materials Science and Engineering at Tsinghua University under the direction of Professor Jing Zhu. He then joined in Beijing National Center

for Electron Microscopy at Tsinghua University. In 2015, he moved to Technical University of Denmark as a postdoc. His research interests include energy storage and conversion, transmission electron microscopy, and microfabrication.

REFERENCES

[1] B. Dunn, H. Kamath, J. M. Tarascon, Science 334 (2011) 928-935.

[2] S. Maiti, A. Pramanik, S. Mahanty, CrystEngComm 18 (2016) 450-461.

[3] A. Walcarius, Chem. Soc. Rev. 42 (2013) 4098-4140.

[4] P. Poizot, S. Laruelle, S. Grugeon, L. Dupont, J. M. Tarascon, Nature 407 (2000) 496-499.

[5] Y. Idota, T. Kubota, A. Matsufuji, Y. Maekawa, T. Miyasaka, Science 276 (1997) 1395-1397.

[6] J. Wang, N. Yang, H. Tang, Z. Dong, Q. Jin, M. Yang, D. Kisailus, H. Zhao, Z. Tang, D. Wang, Angew. Chem. 125 (2013) 1-5.

[7] G. Y. Huang, S. M. Xu, S. S. Lu, L. Y. Li, H. Y. Sun, ACS Appl. Mater. Interfaces 6 (2014) 7236-7243.

[8] S. Bai, M. Cao, Y. Jin, X. Dai, X. Liang, Z. Ye, M. Li, J. Cheng, X. Xiao, Z. Wu, Z. Xia, B. Sun, E. Wang, Y. Mo, F. Gao, F. Zhang, Adv. Energy Mater. 4 (2014) 1301460 (1-6).

[9] J. Liang, H. Hu, H. Park, C. Xiao, S. Ding, U. Paik, X. W. Lou, Energy Environ. Sci. 8 (2015) 1707-1711.

[10] Z. Fan, J. Liang, W. Yu, S. Ding, S. Cheng, G. Yang, Y. Wang, Y. Xi, K. Xi, R.V. Kumar, Nano Energy 16 (2015) 152162.

[11] S. Xu, M. C. Hessel, H. Ren, R. Yu, Q. Jin, M. Yang, H. Zhao, D. Wang, Energy Environ. Sci. 7 (2014) 632-637.

[12] M. V. Reddy, C. Yu, J. Fan, K. P. Loh, B. V. R. Chowdari, ACS Appl. Mater. Interfaces 5 (2013) 4361-4366.

[13] A. Kushima, X. Liu, G. Zhu, Z. Wang, J. Huang, J. Li, Nano Lett. 11 (2011) 4535-4541.

[14] W. Zhang, J. Hu, Y. Guo, S. Zheng, L. Zhong, W. Song, L. Wan, Adv. Mater. 20 (2008) 1160-1165.

[15] R. S. J. Prabakar, Y. H. Hwang, E. G. Bae, S. Shim, D. Kim, S. M. Lah, K. S. Sohn, M. Pyo, Adv. Mater. 25 (2013) 3307-3312.

[16] L. Hu, L. Wu, M. Liao, X. Hu, X. Fang, Adv. Funct. Mater. 22 (2012) 998-1004.

[17] L. Huang, D. Chen, Y. Ding, S. Feng, Z. Wang, M. Liu, Nano Lett. 13 (2013) 3135-3139.

[18] L. Yu, L. Zhang, H. Wu, G. Zhang, X. W. Lou, Energy Environ. Sci. 6 (2013) 2664-2671.

[19] G. Y. Huang, S. M. Xu, Z. H. Xu, H. Y. Sun, L. Y. Li, ACS Appl. Mater. Interfaces 6 (2014) 21325-21334.

[20] L. Huang, H. G. Waller, Y. Ding, D. Chen, D. Ding, P. Xi, Z. Wang, M. Liu, Nano Energy 11 (2015) 64-70.

[21] J. Ma, H. Wang, X. Yang, Y. Chai, R. Yuan, J. Mater. Chem. A 3 (2015) 12038-12043.

[22] M. V. Reddy, C. T. Cherian, K. Ramanathan, K. C. W. Jie, T. Y. W. Daryl, T. Y. Hao, S. Adams, K. P. Loh, B. V. R. Chowdari, Electrochim. Acta 118 (2014) 75-80.

[23] C. T. Cherian, J. Sundaramurthy, M. V. Reddy, P. S. Kumar, K. Mani, D. Pliszka, C. H. Sow, S. Ramakrishna, B. V. R. Chowdari, ACS Appl. Mater. Interfaces 5 (2013) 9957-9963.

[24] M. V. Reddy, C. Yu, J. Fan, K. P. Loh, B. V. R. Chowdari, RSC Adv. 2 (2012) 9619-9625.

[25] X. W. Lou, D. Deng, J. Lee, J. Feng, A. L. Archer, Adv. Mater. 20 (2008) 258-262.

[26] T. K. Nam, D. W. Kim, J. P. Yoo, C. Y. Chiang, Science 312 (2006) 885-888.

[27] V. M. Reddy, S. V. G. Rao, B. V. R. Chowdari, Chem. Rev. 113 (2013) 5364-5457.

[28] C. Yuan, B. Wu, Y. Xie, X. W. Lou, Angew. Chem. Int. Ed. 53 (2014) 1488-1504.

[29] Q. Xie, Y. Ma, D. Zeng, L. Wang, G. Yue, D. Peng, Sci. Rep. 5 (2015) 8351 (1-8).

[30] L. Qiao, X. Wang, L. Qiao, X. Sun, X. Li, Y. Zheng, D. He, Nanoscale 5 (2013) 3037-3042.

[31] M. S. Wu, H. W. Chang, J. Phys. Chem. C 117 (2013) 2590-2599.

[32] L. Ji, Z. Lin, M. Alcoutlabi, X. Zhang, Energy Environ. Sci. 4 (2011) 2682-2699.

[33] C. M. Park, J. H. Kim, H. Kim, H. J. Sohn, Chem. Soc. Rev. 39 (2010) 3115-3141.

[34] I. A. Hochbaum, P. Yang, Chem. Rev. 110 (2010) 527-546.

[35] X. Sun, W. Si, X. Liu, J. Deng, L. Xi, L. Liu, C. Yan, G. O. Schmidt, Nano Energy 9 (2014) 168-175.

[36] X. Gu, L. Chen, Z. Ju, H. Xu, J. Yang, Y. Qian, Adv. Funct. Mater. 23 (2013) 4049-4056.

[37] Y. Wang, H. Xia, L. Lu, J. Lin, ACS Nano 4 (2010) 1425-1432.

[38] T. Y. Wei, C. H. Chen, H. C. Chien, S. Y. Lu, C. C. Hu, Adv. Mater. 22 (2010) 347-351.

[39] L. Hou, L. Lian, L. Zhang, G. Pang, C. Yuan, X. Zhang, Adv. Funct. Mater. 25 (2015) 238-246.

[40] X. Lai, E. J. Halpert, D. Wang, Energy Environ. Sci. 5 (2012) 5604-5618.

[41] L. Wang, Y. Han, X. Feng, J. Zhou, P. Qi, B. Wang, Coordin. Chem. Rev. 307 (2016) 361-381.

[42] X. Xu, R. Cao, S. Jeong, J. Cho, Nano Lett. 12 (2012) 4988-4991.

[43] X. Cao, B. Zheng, X. Rui, W. Shi, Q. Yan, H. Zhang, Angew. Chem. Int. Ed. 53 (2014) 1404-1409.

[44] J. S. Yang, S. Nam, T. Kim, H. J. Im, H. Jung, H. J. Kang, S. Wi, B. Park, R. C. Park, J. Am. Chem. Soc. 135 (2013) 7394-7397.

[45] R. R. Salunkhe, J. Tang, Y. Kamachi, T. Nakato, H. J. Kim, Y. Yamauchi, ACS Nano 9 (2015) 6288-6296.

[46] F. Zou, X. Hu, Z. Li, L. Qie, C. Hu, R. Zeng, Y. Jiang, Y. Huang, Adv. Mater. 26 (2014) 6622-6628.

[47] Z. Guo, M. V. Reddy, B. M. Goh, A. K. P. San, Q. Bao, K. P. Loh, RSC Adv. 3 (2013) 19051-

19056.

[48] D. Farrusseng, S. Aguado, C. Pinel, Angew. Chem. Int. Ed. 48 (2009) 7502-7513.

[49] D. Cai, B. Liu, D. Wang, L. Wang, Y. Liu, B. Qu, X. Duan, Q. Li, T. Wang, J. Mater. Chem. A 4 (2016) 183-192.

[50] Y. C. Lee, Y. S. Bae, C. N. Jeong, K. O. Farha, A. A. Sarjeant, L. C. Stern, P. Nickias, Q. R. Snurr, T. J. Hupp, T. S. Nguyen, J. Am. Chem. Soc. 133 (2011) 5228-5231.

[51] J. Kim, S. A. Hong, J. Yoo, Chem. Eng. J. 266 (2015) 179-188.

[52] S. T. Myung, N. Takahashi, S. Komaba, S. C. Yoon, Y. K. Sun, K. Amine, H. Yashiro, Adv. Funct. Mater. 21 (2011) 3231-3241.

[53] R. T. Paudel, A. Zakutayev, S. Lany, M. d'Avezac, A. Zunger, Adv. Funct. Mater. 21 (2011) 4493-4501.

[54] Y. Sharma, N. Sharma, S. V. G. Rao, B. V. R. Chowdari, Adv. Funct. Mater. 17 (2007) 2855-2861.

[55] X. Wu, P. Jiang, W. Cai, X. D. Bai, P. Gao, S. S. Xie, Adv. Energy Mater. 10 (2008) 476-481.

[56] G. Zhang, X. W. Lou, Adv. Mater. 25 (2013) 976-979.

[57] B. Zhu, N. Liu, M. McDowell, Y. Jin, Y. Cui, J. Zhu, Nano Energy 13 (2015) 620-625.

[58] H. Sun, G. Xin, T. Hu, M. Yu, D. Shao, X. Sun, J. Lian, Nat. Commun. 5 (2014) 4526 (1-8).

[59] J. K. Shon, H. S. Lee, G. O. Park, J. Yoon, E. Park, G. S. Park, S. S. Kong, M. Jin, J. M. Choi, H. Chang, S. Doo, J. M. Kim, W. S. Yoon, C. Pak, H. Kim, G. D. Stucky, Nat. Commun. 7 (2016) 11049 (1-9).

[60] M. V. Reddy, B. L. W. Wen, K. P. Loh, B. V. R. Chowdari, ACS Appl. Mater. Interfaces 5 (2013) 7777-7785.

[61] M. V. Reddy, G. Prithvi, K. P. Loh, B. V. R. Chowdari, ACS Appl. Mater. Interfaces 6 (2014)

680-690.

[62] M. V. Reddy, G. V. S. Rao, B. V. R. Chowdari, J. Mater. Chem. 21 (2011) 10003-10011.

[63] Y. Wu, Y. Wei, J. Wang, K. Jiang, S. Fan, Nano Lett. 13 (2013) 818-823.

[64] G. Y. Huang, S. M. Xu, J. L. Wang, L. Y. Li, X. J. Wang, Acta Chim. Sinica 71 (2013) 1589-1597.

[65] J. Mujtaba, H. Y. Sun, G. Y. Huang, Y. Y. Zhao, H. Arandiyan, G. X. Sun, S. M. Xu, J. Zhu, RSC Adv. 6 (2016) 31775-31781.

[66] G. Y. Huang, S. M. Xu, Y. Yang, H. Y. Sun, Z. H. Xu, RSC Adv. 6 (2016) 10763-10774.

[67] F. Zou, Y. M. Chen, K. Liu, Z. Yu, W. Liang, S. M. Bhaway, M. Gao, Y. Zhu, ACS Nano 10 (2016) 377-386.

[68] W. Guo, W. Sun, Y. Wang, ACS Nano 9 (2015) 11462-11471.

[69] G. Y. Huang, S. M. Xu, S. S. Lu, L. Y. Li, H. Y. Sun, Electrochim. Acta 135 (2014) 420-427.

[70] J. Mujtaba, H. Y. Sun, G. Y. Huang, K. Molhave, Y. G. Liu, Y. Y. Zhao, X. Wang, S. M. Xu, J. Zhu, Sci. Rep. 6 (2016) 20592 (1-8).